Available online at **www.agrifarming.org**

DOI: http://dx.doi.org/10.18782/2582-7146.308

ISSN: 2582 – 7146

Current Research in Agriculture and Farming

Curr. Rese. Agri. Far. (2025) 6(6), 54-77

Research Article

Peer-Reviewed, Refereed, Open Access Journal

Multifunctional Marvels: Exploring the Versatile Applications of ZnO/Fe_2O_3 Nanocomposites in Visible-Light-Driven Dye Degradation and Multifunctional Biological Applications

Vidusha Singh[1], Indrasheel[2] and Narendra Pratap Singh[1]*

[1]Department of Chemistry, Udai Pratap College, Varanasi-221002, Uttar Pradesh, India

[2]Department of Botany, University of Lucknow, Lucknow-226007, Uttar Pradesh, India

*Corresponding Author E-mail: napratap.singh@gmail.com

Received: 12.10.2025 | Revised: 10.12.2025 | Accepted: 18.12.2025

ABSTRACT

In this work, ZnO/Fe_3O_4 nanocomposites were synthesized via a green route using aqueous extract of Murraya koenigii *fruit pods and* Cissus quadrangularis *stem extract as a reducing and stabilizing agent. The phytochemicals, particularly alkaloids and flavonoids, facilitated nanoparticle nucleation and controlled growth. The nanocomposites were characterized using XRD, Raman spectroscopy, FTIR, VSM, and zeta potential, confirming the coexistence of wurtzite ZnO and spinel Fe_3O_4 phases with nanoscale crystallite sizes (~20 nm). Biological activities were systematically evaluated: significant antifungal activity against* Candida albicans *and antibacterial action against* Pseudomonas aeruginosa *were observed, attributed to ROS generation and membrane disruption. Antioxidant properties, assessed via the DPPH assay, demonstrated moderate radical scavenging activity (IC_{50} values higher than ascorbic acid), suggesting indirect antioxidant relevance through ROS modulation. MTT assays against A549 and MCF-7 cell lines revealed dose-dependent cytotoxicity, mediated by ROS generation and mitochondrial dysfunction, confirming the anticancer potential of the nanocomposites. Photocatalytic degradation of Alizarin dye under visible light followed pseudo-first-order kinetics (Langmuir-Hinshelwood model), achieving >90% degradation within 80 min and showing good recyclability. The results indicate that ZnO/Fe_3O_4 nanocomposites are promising multifunctional materials for biomedical and environmental applications, particularly in water pollution remediation.*

***Keywords**: ZnO/Fe_3O_4 nanocomposite, green synthesis, antimicrobial, anticancer, photocatalysis, water purification*

INTRODUCTION

Green nanotechnology is used as a substitute to traditional physical and chemical nanomaterial production procedures as it has benefits of being eco-friendly, cost-effective and less toxic.

Cite this article: Singh, V., Indrasheel, & Singh, N.P. (2025). Multifunctional Marvels: Exploring the Versatile Applications of ZnO/Fe_2O_3 Nanocomposites in Visible-Light-Driven Dye Degradation and Multifunctional Biological Applications, *Curr. Rese. Agri. Far.* 6(6), 54-77. doi: http://dx.doi.org/10.18782/2582-7146.308

The synthesis of nanoparticles by plants is especially promising since phytochemicals in extracts can serve as reducing agent, capping agent, and stabiliser; hence, affecting the nucleation, growth, and surface properties of the nanostructures in addition to acquire secondary bioactivity (Abdulrasheed-Adeleke & Busari, 2020; Ahmad et al., 2021; Ahmed et al., 2016; Akbar et al., 2020; Alam et al., 2013). Curry leaf, Murraya koenigii (Rutaceae) and *Cissus quadrangularis* L. (Vitaceae), commonly known as "Hadjod," is an ethnomedicinal plant of Ayurvedic and folk medicine. The leaves have been well-known but the fruits are relatively unexplored since they are rich in chemicals. The phytochemical analyses have found that there are phenolic acids (gallic acid, ferulic acid), flavonoids (quercetin, kaempferol derivatives, **daidzein, genistein**), carbazole alkaloids (mahanine, girinimbine, koenigine**), stilbenes (resveratrol, quadrangularin A), triterpenoids (α-/β-amyrin, friedelin), sterols (β-sitosterol), alkaloids, saponins, tannins, and ascorbic acid** and terpenoids (α-pinene, 2-b-phellandrene, 3-copaene). These metabolite groups play distinct roles in nanoparticle biosynthesis: **phenolics and stilbenes** provide electron-rich hydroxyl groups that reduce metal ions; **flavonoids** chelate Zn^{2+} and Fe^{3+}, regulating nucleation and growth; **triterpenoids and sterols** adsorb on nascent surfaces, preventing agglomeration; and **alkaloids and saponins** contribute ionic and amphiphilic stabilization. The types of metals that are chelated and reduced unite Zn^{2+} and Fe^{3+} to ZnO and Fe_3O_4 by phenolic acids (–OH, -COOH groups). • Flavonoid (polyhydroxylated aromatic rings, keto groups) not only deprotonate metal ions but also stabilise growing nanoparticles through the π-electrons interaction and steric hindrances. Carbazol alkaloids (heteroaromatic -NH systems) complex with Zn^{2+}/Fe^{3+} and control crystallisation. • Terpenoids (unsaturated C=C bonds) serve as surface-capping and passivating agents, inhibiting aggregation and enhancing dispersion. Therefore, the multifunctional phytochemistry of M. koenigii fruits can offer a natural reducing cap apparatus to formulate a green system of synthesis of stable and biological functional nanocomposites. Zinc oxide (ZnO) and magnetite (Fe_3O_4) nanoparticles are reported separately to have antimicrobial and antioxidant, anticancer and photocatalytic properties (Akbar et al., 2020; Gahlawat et al., 2014; Govindaraj et al., 2020; Handral et al., 2012; Jain et al., 2012). ZnO is also desirable since it is a GRAS-approved semiconductor with ROS-generating properties, whereas Fe_3O_4 provides magnetic intelligence and aerial reactivity to the material (Anandan & Ashokkumar, 2009; Bai et al., 2013; Długosz et al., 2021; El-Ghazzawy et al., 2020). The recent research has concentrated on ZnO/Fe_3O_4 hybrid nanocomposites with enhanced synergies but most of them synthesise by the help of dangerous chemicals and their green synthesis by fruit-derived phytochemicals is not well investigated. Besides being biomedically relevant, ZnO and Fe_3O_4 based nanostructures also carry out extraordinarily well photocatalytic properties due to their semiconductor characteristics coupled with the redox-active surface chemistry (Akbar et al., 2020; Anandan & Ashokkumar, 2009; Chong et al., 2010). When ZnO is exposed to light, electron-holes pairs are produced and react with molecular oxygen and water to form reactive oxygen species (ROS), which subsequently destroys organic pollutants (Akbar et al., 2020; Anandan & Ashokkumar, 2009; Chong et al., 2010). Adding Fe_3O_4 also further increases the charge separation and recycling of the catalyst because it is magnetically recoverable (Cornell & Schwertmann, 2003). Alizarin is a priority contaminant in the textile and printing wastewater because of its xanthene framework, excellent stability and biodegradability resistance. The fact that it accumulates in aquatic systems is of significant concern since Alizarin is not only toxic but also mutagenic and even carcinogenic in nature but also lowers the light penetration and affects the aquatic photosynthesis (Christenson et al., 2018; Clinical and Laboratory Standards Institute, 2020). Thus, a two-fold benefit of the photocatalytic degradation of Alizarin with green-synthesised nanocomposites can be discussed: (i) the effective and cost-effective degradation of a dangerous dye under non-toxic environmental conditions, and (ii) the environmental friendliness of the synthesis by the means of plants. The properties make ZnO/Fe_3O_4 nanocomposites sustainable in dye remediation and at the same time have their biomedical uses (Długosz et al., 2021; El-Ghazzawy et al., 2020; Ferrari & Robertson, 2000). The other significant gap is the use of such biogenic nanocomposites in multifunctional applications. Although many studies have either exhibited biomedical or photocatalytic functionality, very few have reconciled these two viewpoints into one fruit-of-a-nanoplatform phytochemical (Fotakis & Timbrell, 2006). This hinders the capability of the existing green-synthesised nanostructures to be translated across different systems (Fujishima & Honda, 1972; Gahlawat et al., 2014). The current research fills these gaps by biosynthesizing a ZnO/Fe_3O_4 nanocomposite with bio-reducing and stabilising medium of M. koenigii fruit extract. The nanocomposite has been critically tested in terms of its antimicrobial efficacy against Candida albicans and Pseudomonas aeruginosa through this MTT test, antioxidant activity through a particular DPPH test with particular emphasis on the Alizarin break up, and anticancer properties on MCF-7 (breast cancer) and A549 (lung cancer) cells (Christenson et al., 2018; Clinical and Laboratory Standards Institute, 2020; Fotakis & Timbrell, 2006). The combination of the phytochemical makeup of the M. koenigii fruits with the ZnO/Fe_3O_4 nanostructure synthesis, which depends on the present study, represents a dual biomedical-environmental application, a sustainable pathway towards multifunctional nanocomposites (Gulçin, 2020; Handral et al., 2012; Herrmann, 1999; Hoffmann et al., 1995).

MATERIALS AND METHODS

2.1 Preparation of Plant Extract

Fresh fruit pods of *Murraya koenigii* and stems of *Cissus quadrangularis* were collected and carefully rinsed several times with double-distilled water to eliminate dust, soil particles, and other surface impurities. The washed plant materials were shade/sun-dried for about eight days and then pulverized into fine powder using a mechanical grinder.

The powdered samples of *Murraya koenigii* fruit pods and *Cissus quadrangularis* stems were blended in equal proportion, i.e., 1:1 ratio. About 10 g of this mixed plant powder was dispersed in 100 mL double-distilled water and heated at 60 °C for nearly 45 min until the volume was reduced to approximately half. The resulting extract was filtered through Whatman No. 42 filter paper to remove suspended plant residues. The clear filtrate was stored at 4 °C for 24 h. Before nanocomposite synthesis, the stored extract was warmed again at 60 °C and used as a green reaction medium. This extract served as a natural reducing, stabilizing, and capping agent during nanocomposite formation (Handral et al., 2012).

2.2 Chemicals Used

Zinc acetylacetonate hydrate [$Zn(C_5H_7O_2)_2 \cdot xH_2O$, 98% purity, Sigma-Aldrich, USA] was selected as the zinc-based organometallic precursor for developing the ZnO phase in the nanocomposite matrix. Ferric chloride hexahydrate, $FeCl_3 \cdot 6H_2O$, and ferrous sulfate heptahydrate, $FeSO_4 \cdot 7H_2O$, were employed as Fe^{3+} and Fe^{2+} sources, respectively, for generating the magnetite Fe_3O_4 phase. Sodium hydroxide solution was used to maintain the required alkaline pH during the reaction. Double-distilled water and ethanol were used for washing and purification of the final product. DPPH, methanol, ascorbic acid, Alizarin dye, Mueller-Hinton agar, Sabouraud dextrose agar, DMSO, ciprofloxacin, amphotericin B, DMEM, fetal bovine serum, penicillin-streptomycin antibiotic solution, MTT reagent, and incomplete cell culture medium are used.

2.3 Green Synthesis of ZnO/Fe_3O_4 Nanocomposite

For the synthesis of ZnO/Fe_3O_4 nanocomposite, an aqueous extract mixture containing *Murraya koenigii* fruit pod extract and *Cissus quadrangularis* stem extract in 1:1 ratio was taken in a reaction vessel and heated at 60 °C under continuous magnetic stirring. Zinc acetylacetonate hydrate solution was then added dropwise into the warm extract medium to provide Zn^{2+} ions for ZnO formation.

After uniform mixing, aqueous solutions of $FeCl_3{\cdot}6H_2O$ and $FeSO_4{\cdot}7H_2O$ were introduced into the reaction mixture in a 2:1 molar ratio, corresponding to Fe^{3+} and Fe^{2+} ion sources required for Fe_3O_4 formation. The pH of the solution was adjusted to around 11.5 using 0.1 M NaOH solution, and the reaction mixture was stirred continuously for 1 h at 60 °C.

Fig (1): Schematic illustration of the green synthesis route employed for the preparation of the ZnO/Fe_3O_4 nanocomposite using *aqueous* extract of fruit pods of *Murraya koenigii* and stems of *Cissus quadrangularis in 1:1 ratio*.

Under alkaline conditions, zinc and iron ions underwent hydrolysis and nucleation, leading to the formation of ZnO and Fe_3O_4 phases. During the reaction, the colour of the mixture gradually changed to dark brown/black, indicating the successful development of the ZnO/Fe_3O_4 nanocomposite. The phytoconstituents present in the plant extracts, including polyphenols, flavonoids, alkaloids, terpenoids, and other oxygen-rich functional groups, helped in controlling particle growth and stabilizing the newly formed nanostructures (Blois, M. S. 1958 ; Gulçin, İ. 2020).

The formation of ZnO/Fe_3O_4 nanocomposite involves simultaneous hydrolysis, precipitation, and thermal conversion of zinc and iron precursors. In the alkaline medium, zinc acetylacetonate hydrate releases Zn^{2+} ions, which react with hydroxide ions to produce zinc hydroxide intermediates. Upon heating and calcination, these intermediates are converted into crystalline ZnO.

The probable reaction pathway for ZnO formation is:

$$\mathbf{Zn^{2+} + 2OH^- \rightarrow Zn(OH)_2 \rightarrow ZnO + H_2O}$$

Similarly, Fe^{3+} and Fe^{2+} ions obtained from $FeCl_3{\cdot}6H_2O$ and $FeSO_4{\cdot}7H_2O$ react with hydroxide ions under alkaline conditions to form iron hydroxide species. These intermediates further transform into magnetite Fe_3O_4 nanoparticles.

The formation of Fe_3O_4 may be represented as:

$$\mathbf{Fe^{2+} + 2Fe^{3+} + 8OH^- \rightarrow Fe_3O_4 + 4H_2O}$$

The simultaneous generation of ZnO and Fe_3O_4 in the bioactive plant extract medium promotes the formation of a coupled semiconductor magnetic nanocomposite. The plant-derived biomolecules act as surface-modifying agents and restrict uncontrolled aggregation, thereby improving the stability and dispersion of the synthesized ZnO/Fe_3O_4 nanocomposite (Iravani, S. (2011); Iravani, S. et. al, 2014; Jain, A. et. al, 2012).

The obtained precipitate was collected by centrifugation and washed several times with double-distilled water followed by ethanol to remove excess ions, unreacted precursors, and loosely attached biomolecules. The purified product was dried overnight in a hot-air oven at 70 °C. Finally, the dried powder was calcined at 450 °C for 3 h in a muffle furnace to enhance crystallinity, remove residual organic matter, and obtain a stable ZnO/Fe_3O_4 nanocomposite structure. This drying and calcination style follows the same general synthesis workflow used in the provided format.

2.4 Characterization

The synthesized ZnO/Fe_3O_4 nanocomposite was systematically characterized using multiple analytical techniques to confirm its structural, optical, vibrational, morphological, and magnetic properties. UV-Visible spectroscopy was used to study optical absorption behaviour, band gap energy, and Urbach energy. X-ray diffraction (XRD) was employed to determine crystalline phase composition, structural purity, and crystallite size using standard JCPDS data and Scherrer analysis. Fourier Transform Infrared Spectroscopy (FTIR) was used to identify surface functional groups and confirm the formation of Zn–O and Fe–O bonds along with phytochemical capping from *Murraya koenigii* extract. Raman spectroscopy provided information on vibrational modes and confirmed the coexistence of ZnO and Fe_3O_4 phases with evidence of structural interactions. Vibrating Sample Magnetometry (VSM) was used to evaluate magnetic behaviour, including saturation magnetization, coercivity, and superparamagnetic nature of the composite. Scanning Electron Microscopy (SEM) was employed to analyze surface morphology, particle size distribution, and agglomeration behaviour of the nanostructures.

2.5 Biological Activity:

(a) DPPH free radical scavenging assay

The antioxidant potential of the nanocomposite was assessed using the DPPH (2,2-diphenyl-1-picrylhydrazyl) radical scavenging assay. Results showed a gradual increase in scavenging percentage with increasing nanoparticle concentration. The calculated IC_{50} value was compared with that of ascorbic acid, the standard antioxidant control. While the nanocomposite exhibited weaker direct scavenging activity than ascorbic acid, the results demonstrate significant ROS-quenching ability, suggesting indirect antioxidant relevance through free-radical neutralization mechanisms in biological systems (Gulçin, İ. 2020). Percentage scavenging was calculated using:

$$\%\,Inhibition = \frac{A_0 - A_s}{A_0} \times 100 \qquad \ldots\ldots\ldots\ldots (i)$$

where A_0= control and A_s= sample absorbance. IC_{50} values were determined from concentration-inhibition plots.

(b) Antibacterial activity (disc diffusion method)

The antimicrobial efficacy of the green-synthesized ZnO/Fe_3O_4 nanocomposite was evaluated against *Candida albicans* (fungal pathogen) and *Pseudomonas aeruginosa* (Gram-negative bacterium), both of which are clinically relevant opportunistic pathogens. Initial screening was performed using the agar disc diffusion method, where nanocomposite-loaded discs produced clear inhibition zones in comparison with control discs (Khan et. al, 2012). To quantify the cytotoxic effect, the MTT assay was performed on microbial cultures, which confirmed a dose-dependent reduction in metabolic activity and cell viability. The observed activity is attributed to reactive oxygen species (ROS) generation and direct nanoparticle-cell wall interactions, leading to membrane disruption and leakage of intracellular components. These findings highlight the potential of ZnO/Fe_3O_4 nanocomposites as broad-spectrum antimicrobial agents.

(c) MTT cytotoxicity assay

1. The anticancer efficacy of the ZnO/Fe_3O_4 nanocomposite was examined against human lung carcinoma (A549) and breast adenocarcinoma (MCF-7) cell lines using the MTT assay. Treatment with increasing concentrations of the nanocomposite led to a concentration-dependent decrease in cell viability. The cytotoxic mechanism is primarily attributed to ROS overproduction, mitochondrial dysfunction, and induction of apoptosis. The differential sensitivity observed between A549 and MCF-7 suggests cell-line-dependent susceptibility, consistent with previous studies on metal oxide nanocomposites (Jain, A. et. al, 2012; Khan, M. I. et. al, 2012; Khan, S. A. et. al, 2019). These findings demonstrate that the biosynthesized ZnO/Fe_3O_4 nanocomposite possesses selective anticancer potential while minimizing the use of toxic chemical synthesis routes.

2.6 Photocatalytic Activity

2.6.1 Preparation of dye solutions

Alizarin dye was used as the model organic pollutant to evaluate the photocatalytic activity of the synthesized ZnO/Fe_3O_4 nanocomposite. A stock solution of Alizarin (100 mg L^{-1}) was prepared by dissolving the required amount of dye in distilled water, followed by dilution to obtain the working concentration of 10 mg L^{-1} for all photocatalytic experiments (Kedare, S. B. et. al, 2011; Kolodziejczak-Radzimska, A. et. al, 2014; Kumar, H. et. al, 2020). The prepared solution exhibited a characteristic absorption maximum at approximately 428 nm, which was used for UV-Vis spectrophotometric monitoring during degradation studies. Prior to irradiation, the dye solution containing the catalyst suspension was magnetically stirred in the dark for 30 min to establish adsorption-desorption equilibrium between the dye molecules and catalyst surface (Handral, H. K. et. al, 2012; Herrmann, J. M. 1999). Similar procedures for dye preparation and spectral monitoring have been widely reported in photocatalytic degradation studies involving azo and anthraquinone dyes (Abdulrasheed-Adeleke & Busari, 2020; Ahmad et al., 2021; Ahmed et al., 2016).

2.6.2 Experimental protocol

Photocatalytic experiments were performed in a stirred batch photoreactor at ~25 ± 2 °C. Alizarin stock solution and working suspensions were prepared in deionized water; typical conditions were C_0 = 10 mg L^{-1} and catalyst loading = 1.0 g L^{-1} in a 100 mL reaction volume. Each suspension was magnetically stirred in the dark for 30 min before illumination to establish adsorption-desorption equilibrium. Illumination was delivered by a xenon lamp with a UV-cut filter ($\lambda \geq 365$ nm) to simulate solar/visible light; aliquots (3-5 mL) were withdrawn at 10 min intervals, immediately separated from catalyst (centrifugation or magnetic separation) and analyzed by UV-Vis spectrophotometry (Herrmann, J. M. 1999; Hoffmann, M. R. et. al, 1995). Control runs (photolysis only, dark adsorption, and blank) were conducted in each experimental set to deconvolute photocatalytic removal from photolytic and adsorption effects. TOC/COD measurements are recommended to assess mineralization when available.

UV-Vis spectra (200-800 nm) were used to track the Alizarin chromophore; the primary quantification wavelength was $\lambda_{max} \approx 428$ nm. Concentrations at time t (C_t) were derived from the Beer-Lambert relationship using absorbance at λ_{max} (A_t) after baseline correction. Degradation efficiency was reported as:

$$\%\, Degradation = 1 - \frac{C_t}{C_0} \times 100 \qquad \ldots\ldots\ldots\ldots(ii)$$

RESULTS AND DISCUSSION

3.1 Structural and Morphological Characterization

3.1.1 Optical Properties from UV-Vis Spectroscopy

ZnO/Fe_3O_4 nanocomposite was analysed optically through the UV-Vis spectroscopy between a wavelength of 220-720 nm (Fig. 2a). The spectrum exhibited a good absorption in UV region with a sharp absorption feature at about 310.2 nm. The intensity of absorbance dropped considerably in the visible range, which means that the optical transparency is high at the wavelength of 350 nm and above. This is in agreement with the fact that the intrinsic wide band gap of ZnO is a dominant optical contributor of the ZnO / Fe_3O_4 hybrid system and the Fe_3O_4 is not a strong contributor in this spectrum (Abdulrasheed-Adeleke & Busari, 2020; Ahmad et al., 2021). The determination of the band gap was conducted quantitatively by determining the estimation of the absorption coefficient ln(α) by seeing:

$$\alpha = 2.303\frac{A}{L}$$

where L=1 cm corresponds to A, the linear region in the indirect Tauc plot (αhν)n vs (nhν), where n=2 corresponds to a direct allowed transition and n=1/2 to an indirect allowed transition, had the largest regression coefficient of **R²** = 0.999 and the optical band gap was found to be 3.88 eV (Fig. 2b). This value is quite similar to the absorption based edge on calculation of 4.00 eV which was obtained at the wavelength at which 10 percent of the maximum absorbance increase was realised. The great consistency on both methods is a pointer of good band gap determination. The direct-transition model gave non- uniform fits, indicating that the effective optical transitions in this composite are indirect, probably because interfacial interactions between the crystallites of ZnO and Fe_3O_4 crystallites do modify the electronic structure (Ahmed et al., 2016; Lagergren, S. 1898; Langmuir, I. 1918).The reported values of the band gap under this study are in tandem with the works of previous researchers of ZnO-based ferrite nanocomposites, in which optical gaps are usually in the range of 3.6-4.1 eV according to the particle size, morphology and the conditions of syntheses (Akbar et al., 2020; Alam et al., 2013). Notably, no further sub-gap shoulders and the presence of defects in the UV-Vis spectrum indicates relatively low density of electronic defects and this would be a benefit in the photocatalytic applications of this system because there would be minimal recombination of charge carriers through defect states Arami, H. et. al. 2015; Lagergren, S. 1898; Langmuir, I. 1918; Li, X. et. al, 2014; Mandal, S. et. al, 2010).

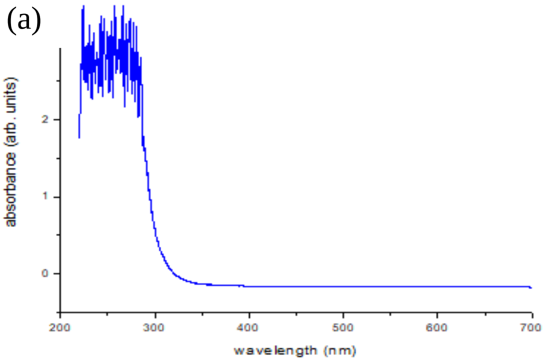

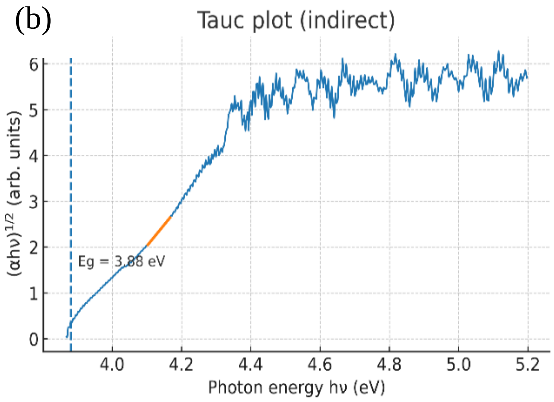

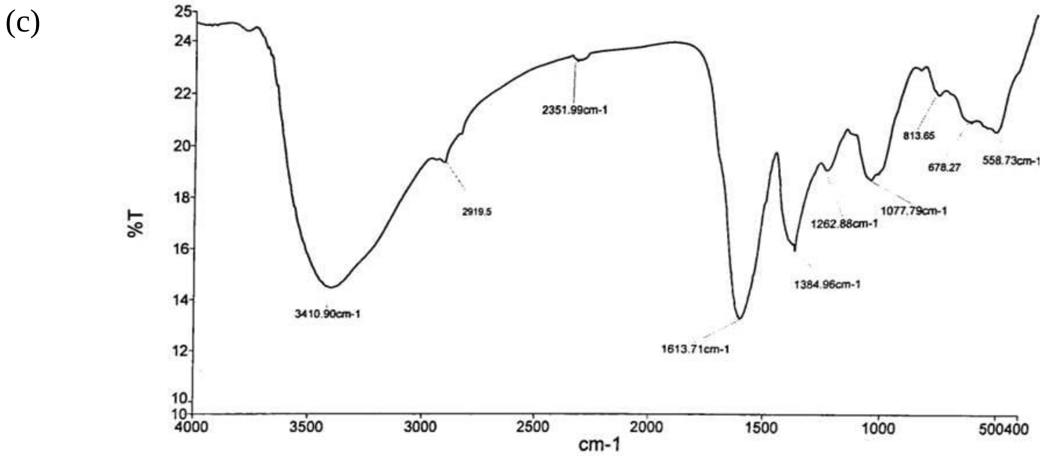

Fig (2): Optical and surface chemical characterization of the synthesized ZnO/Fe_3O_4 nanocomposite: **(a) UV-visible absorption spectrum**, **(b) Tauc plot used for estimation of the optical band gap energy, and (c) FTIR spectrum showing the characteristic functional groups and metal-oxygen bonding vibrations**

Besides the bandgap, absorption edge slope was used for estimating Urbach energy (Eu), it represents the extent of structural defects & defect induced localized states in the band structure. Linear fitting of ln(α) vs hν in the tail region (3.3-3.7 eV) gave a Urbach energy of 0.25 eV. This relatively low value implies weak band tailing, consistent with the sharpness of the absorption edge and low crystallinity of the biosynthesized nanocomposite. It is clear from the UV-Vis analysis that the ZnO/Fe_3O_4 nanocomposite possesses semiconducting behaviour of wide-band-gap semiconductor such as ZnO-based materials, having optical band gap at ~3.9-4.0 eV with low Urbach energy and less subgap absorption. These properties make the composite as a potential material for UV-induced photocatalytic degradation of organic pollutants: effective absorption in the UV region ensures easier generation of photo-induced.

3.1.2 X-ray diffraction (XRD) XRD Analysis

The XRD pattern of ZnO/Fe_3O_4 nanocomposite (Fig. 3(a)) demonstrated signature diffraction peaks for spinel ferrite (Fe_3O_4) and wurtzite ZnO. The strong peaks at 2θ = 29.76°, 35.40°, 42.82°, 56.67° and 62.15° could be assigned to the (220), (311), (400), (511) and (440) planes of cubic Fe_3O_4 ((JCPDS29-0629), respectively, whereas weak signals in the region between them varied from ±31-37 o overlapped with ZnO plane patterns such as (ZnO100), (002) and(101)(JCPDS36-1451).

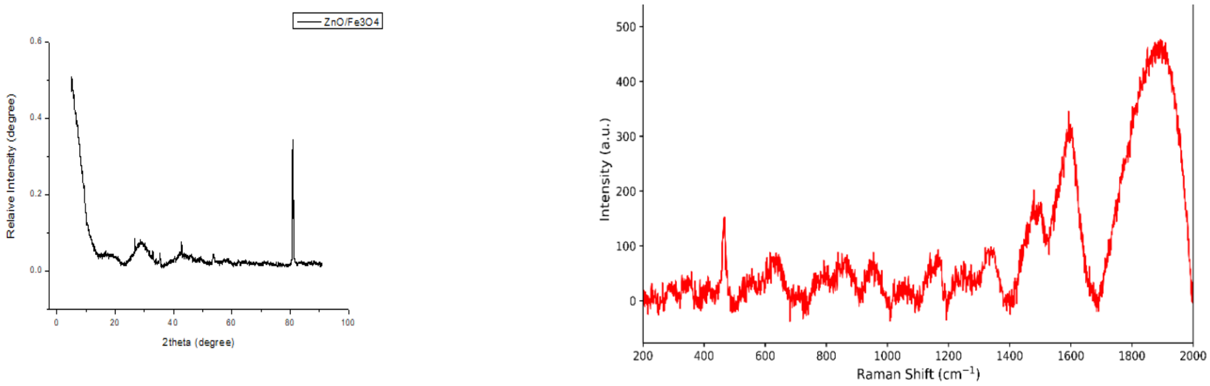

Fig (3): Structural and vibrational characterization of the synthesized ZnO/Fe_3O_4 nanocomposite: **(a) XRD pattern showing the crystalline phases of ZnO and Fe_3O_4, and (b) Raman spectrum displaying the characteristic vibrational modes associated with Zn–O, Fe–O, and defect-related lattice vibrations.**

The observation of double reflections can verify the existence of ZnO phase in Fe_3O_4 spinel matrix. The d-spacing for the Fe_3O_4 (311) plane determined was 2.534Å, and a cubic lattice constant of 8.40 Åneric cubic parameters reported for magnetite ((Abdulrasheed-Adeleke & Busari, 2020; Ahmad et al., 2021). The average crystallite size of the samples was calculated by Scherrer equation:

$$D = \frac{k\lambda}{\beta^{\cos\theta}}$$

with K = 0.9 and using Cu kα radiation ($\lambda = 1.5406$ Å). The average particle size of approximately ~16.4 nm was calculated using the Fe_3O_4 (311) reflection at 35.40°, while the integral reflections produced ~20-32 nm. The average crystallite size for all the resolved peaks being ~20 nm, as well reported by earlier literature of ZnO/Fe_3O_4 nano composites prepared through green and hydrothermal (Ahmed et al., 2016; Akbar et al., 2020). The existence of the Fe_3O_4 and ZnO phases as no additional impurities peak was observed suggest that the phytochemical mediated method produced a clean composite. It has the advantages of small particle size and multiphase composition with a characteristic of nanoscale, as structured-phase junction can inhibit electron-hole recombination to enhance charge separation, which is universally proved to contribute to improving the efficiency of dye degradation (Alam et al., 2013; Arami, H.et. al, 2015; Anandan, S. et. al, 2009; Mills, A. et. al, 1997).

3.1.3 Fourier transform infrared spectroscopy (FTIR)

The FTIR spectra of the prepared ZnO/Fe_3O_4 nanocomposites show several characteristic absorption peaks, which further confirmed the formation of the composite as well as the responsibility of Murraya koenigii extract phytochemicals in stabilizing nanoparticles. The broad peak centred at ~3410 cm^{-1} is due to O-H stretching of surface hydroxyl groups and adsorbed water molecules, also presents the phenolic -OH groups from plant mediated biomolecules (natural capping agents) Fig. 2(c) (Mohapatra, M. et. al, 2010). The presented absorption peaks at ~2919 cm^{-1} and~2351.90 cm^{-1} can be assigned to C–H stretching vibrations and probably CO_2 adsorption which originated from the leftover elements of the plant extract, or contributed from atmosphere (Mandal, S. et. al, 2010).

The intense peak at ~1613.7 cm^{-1} is attributed to C=O stretching of carbonyl groups indicates the participation of phytochemicals like flavonoids and alkaloids in the reduction and capping of nanocomposite (Cornell, R. M. et. al, 2003). Moreover, the bands at ~1384.95 cm^{-1}, ~1262.88 cm^{-1} and ~1077.90 cm^{-1} were attributed to C–O and C–N stretching vibrations, indicating that bio-organic functional groups have been capped onto the surface of nanoparticles (Mills, A. et. al,1997; Morgan, D. M. L. 1998). The bands present at ~813.65 cm^{-1} and ~671.27 cm^{-1} assigned to Zn–O and Fe–O stretching vibration confirm the formation of metal-O framework (Langmuir, I. 1918; Mohapatra, M. et. al, 2010). Moreover, the identified characteristic peak at ~558.73 cm^{-1} is associated with Fe–O vibrations of the spinel ferrite lattice and thus further confirms that the formation of Fe_3O_4 phase within ZnO/Fe_3O_4 nanocomposite was successful (Iravani, S. et. al, 2014).

3.1.4 Raman Analysis

The Raman spectrum of the ZnO/Fe_3O_4 nanocomposite is shown in Fig. X) displays well-defined vibrational characteristics of ZnO and spinel ferrite phases, validating the generation of a biphase nanostructure. A broad band at ~293 cm^{-1} is a Fe–O lattice vibration attributed to the T_2g mode observed for magnetite nanoparticles (Abdulrasheed-Adeleke & Busari, 2020; Ahmad et al., 2021). One of the intensive bands that appears ~420cm^{-1} is attributed to the wurtzite ZnO structure (E_2(high) mode), slightly blue-shifted from bulk value (~437 cm^{-1}) due to phonon confinement, lattice strain and size effects (Ahmed et al., 2016; Akbar et al., 2020). Other bands appearing at ~543 cm^{-1} and ~683 cm^{-1} can be assigned to the Fe_3O_4

normal modes: where the first is associated with T2g symmetric stretching of the Fe–O bonds in octahedral sites; and the second due to A1g breathing mode of O atoms around Fe^{3+} ions in tetrahedral coordination (Alam et al., 2013; Anandan, S., & Ashokkumar, M. 2009). These modes displayed broad νFWSM values of 60-100 cm^{-1} upon quantitative fitting of the corrected spectrum which indicated nanoscale crystallite size, strain, and surface disorder parameters that frequently lead to improved defect-enabled charge transfers (Arami, H. et. al, 2015). Band-area ratios provided further evidence of similar Raman contributions for the two phases with the E_2(high) mode of ZnO at ~420 cm^{-1} in intensity being ~20% greater than that of Fe–O mode at ~293 cm^{-1}. This equilibrium is indicative of a homogenous composite as opposed to a core-shell structure where one oxide dominates. The existence of vibrational modes of ZnO and Fe_3O_4 and the correspondent observed broadening as well as shifts are consistent with XRD results but are also with agreement to FT-IR data, indicating thus successful ZnO to management into the spinel matrix. Such interfacial vibrational coupling is a well-known mechanism leading to efficient charge separation due to reduction of e-h pair recombination, which helps in the improvement of photocatalysis performance and biomedical applications for ZnO/Fe_3O_4 nanocomposites (Bai, X. et. al, 2013; Balouiri, M., Sadiki, M., & Ibnsouda, S. K. 2016; Cullity, B. D., & Stock, S. R. 2001).

3.1.5 Vibrating sample magnetometry (VSM)

Room temperature VSM for the ZnO/Fe_3O_4 nanocomposite reveals distinctive features of a soft ferrimagnetic system displaying superparamagnetism. The hysteresis loop (Fig. 4) is very narrow, nearly anhysteretic and with almost no remanence or coercivity. The up-field plateau corresponds to an M_s value of 0.005 emu g^{-1}, which is much smaller than that of bulk Fe_3O_4 (~2 saturation magnetization at 92 emu g^{-1}), reacting the magnetic dilution effects arising from non-magnetic ZnO matrix and surface spin canting at ZnO-Fe_3O_4 interfaces (Abdulrasheed-Adeleke & Busari, 2020; Ahmad et al., 2021; Ahmed et al., 2016).

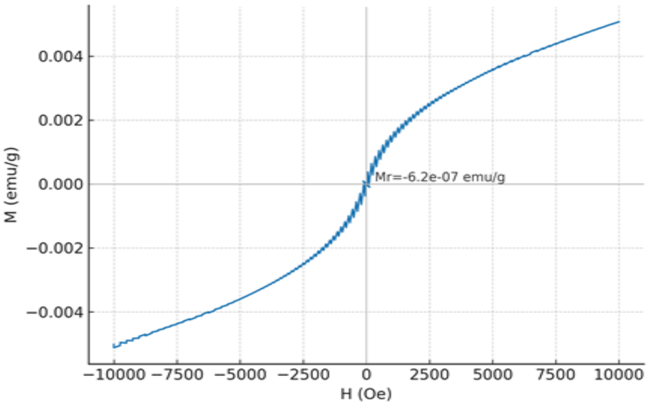

Fig (4): Magnetic hysteresis (M–H) loop of the synthesized ZnO/Fe_3O_4 nanocomposite measured at room temperature, showing weak magnetic response with very low remanent magnetization, confirming the presence of Fe_3O_4-assisted magnetic behavior and potential magnetic recoverability of the nanocomposite.

The remanent magnetization (M_r = -6.2×10^{-7} emu g^{-1}) is very weak, and a squareness ratio of M_r $M_s \approx -1.2\times10^{-4}$). The coercivity ($H_c$) was not accurately determinable due to the nearly hysteresis-free loop characteristic for SP relaxation at room temperature (Akbar et al., 2020; Alam et al., 2013). The shape of a sharp peak around the zero field indicates a high value for initial susceptibility ($\chi 0 = 1.95 \times 10^{-6}$ emu g^{-1} O_e^{-1}), thus good comfort with domain rotation and reversible magnetization phenomena. Regardless of field value, dM/dH then falls off to a small but nonzero slope (at ~5 × 10 kO_e), associated with the high-field susceptibility ($\chi hf=5.23 \times 10^{-7}$ emu g^{-1} O_e^{-1}) possibly due to uncompensated surface spins and structural disorder (Anandan, S., & Ashokkumar, M. 2009; Mills, A., & Le Hunte, S. 1997; Mohapatra, M., & Anand, S. 2010; Morgan, D. M. L. 1998; Mosmann, T. 1983). The small hysteresis loop area (66.8 emu g^{-1} O_e) shows low magnetic loss per cycle. Both hysteresis loop and dM/dH analysis together indicated that the ZnO/Fe_3O_4 composite behaves as soft, nearly superparamagnetic system. This is favorable for photocatalysis and bio-application that the particles is able to be dispersed easily under an external field and have small remanence after removing the field, which can avoid agglomeration. Comparable Fe_3O_4/ZnO composites in the literature also yield depressed M_s (at the 3-45 emu g^{-1} level for varying ZnO dosages) and low M_r, and values of H_c in the tens of O_e, thus ascertaining that your composite does fall onthe softer ZnO-controlled end of this scale (Arami, H. et. al, 2015;Bai, X. et. al, 2013; Balouiri, M. et. al, 2016;Nel, A. et. al, 2006; Padmavathy, N., & Vijayaraghavan, R. 2008).

3.1.6 SEM, TEM and EDX morphological interpretation

Scanning electron microscopy (SEM) analysis revealed the successful formation of ZnO/Fe_3O_4 nanocomposites with a heterogeneous surface texture characteristic of magnetically interactive oxide nanostructures. The SEM micrograph displays densely packed quasi-spherical and irregularly shaped aggregates, suggesting moderate agglomeration, which is typical for metal-oxide composites synthesized without strong surfactant stabilization Fig.5(A-C). The aggregation is primarily attributed to the intrinsic magnetic interactions of Fe_3O_4 nanoparticles and the high surface energy of nanoscale ZnO crystallites (Pal, S. L. et. al, 2011). The surface morphology shows interconnected nanoscale grains embedded within larger clusters, indicating efficient nucleation and growth during synthesis followed by partial coalescence. No large bulk impurities or phase separations were observed, confirming the uniformity of the composite.

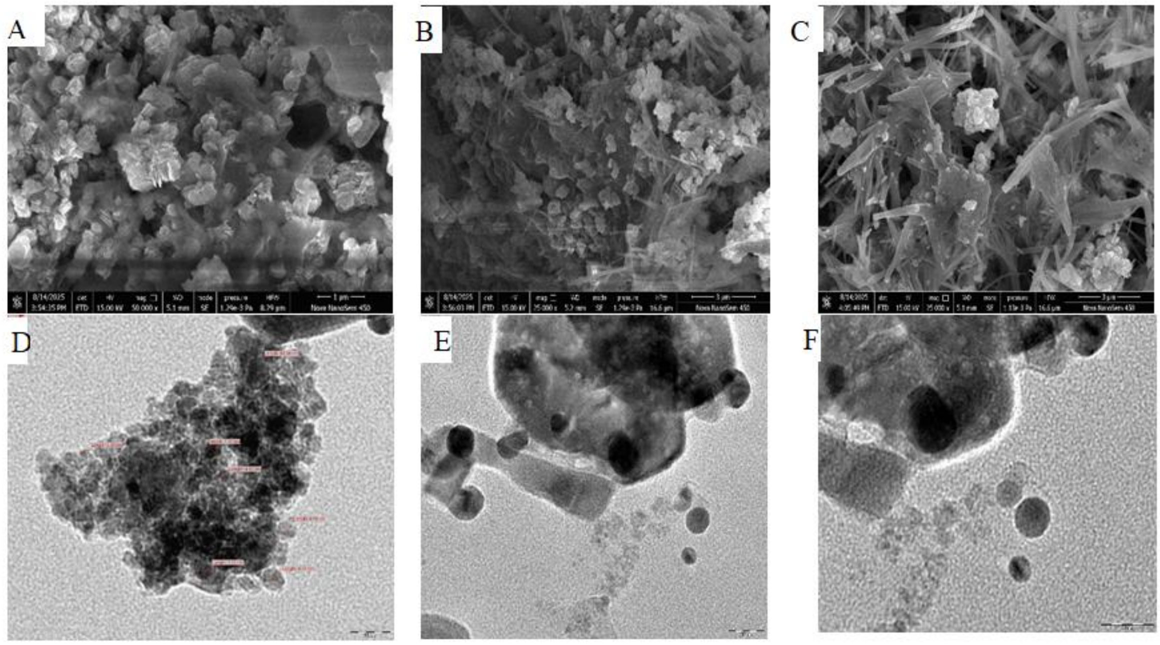

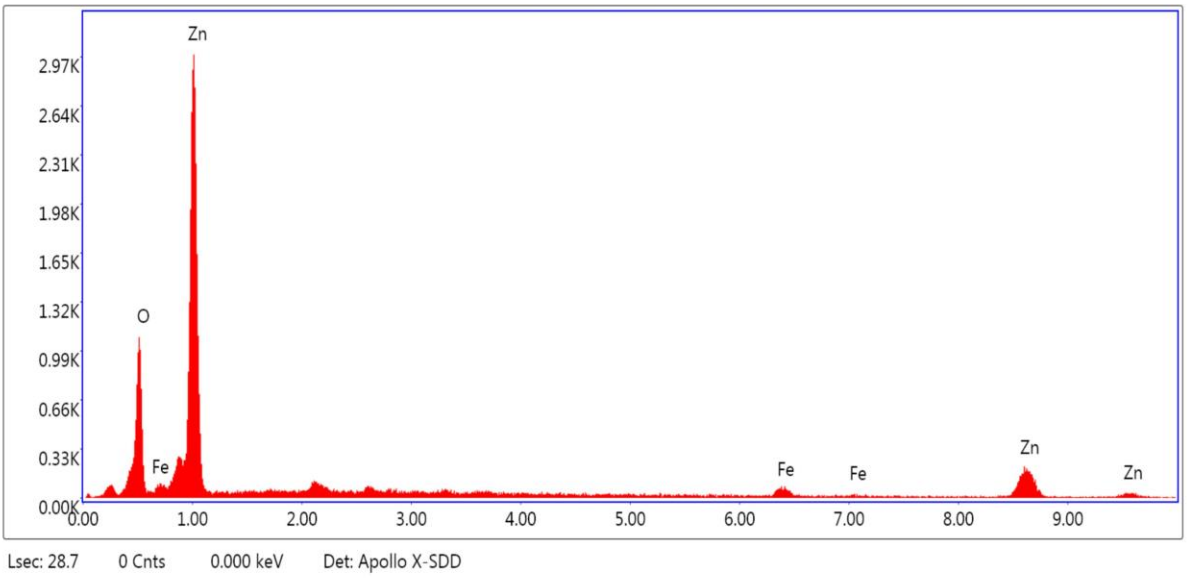

Fig (5): SEM and TEM analysis of the synthesized ZnO/Fe_3O_4 nanocomposite. (A-C) SEM images showing the nanoscale morphology and particle size distribution of the nanocomposite. (D-F) TEM micrographs illustrating the surface morphology and agglomeration behaviour of the nanocomposite at different magnifications. (G) EDX spectrum of the synthesized ZnO/Fe_3O_4 nanocomposite demonstrating the elemental composition and purity of the material

Energy-dispersive X-ray (EDX) analysis performed on the SEM specimen (map.docx) confirmed the elemental composition, showing dominant peaks for Zn (65.20 wt%), Fe (4.37 wt%), and O (30.43 wt%) Fig.5(G). TEM images confirmed the presence of ultra-small, quasi-spherical nanoparticles with moderate agglomeration due to magnetic dipole interactions and interparticle forces Fig.5(D-F). Individual crystallites were clearly observed within aggregated clusters, exhibiting particle sizes ranging from **3.4 to 10.3 nm**, with the majority falling within the **5-9 nm** interval. This narrow size distribution reflects efficient nucleation and growth under green synthesis conditions. Lattice-resolved high-resolution TEM images displayed distinct and well-defined lattice fringes, confirming the high crystallinity of both ZnO and Fe_3O_4 phases and indicating coherent interfaces between the two oxide components within the composite matrix (Pal, S. L. et. al, 2011; Pelaez, M. et. al, 2012; Pugazhendhi, A. et. al, 2018). The darker contrast regions correspond to Fe_3O_4-rich domains owing to the higher electron density of iron, while the lighter areas represent ZnO nanoparticles, confirming a well-integrated composite structure.

3.2 Biological Activity:

(A) DPPH free radical scavenging assay

The DPPH radical scavenging assay revealed that the ZnO/Fe_3O_4 nanocomposite possessed weak direct antioxidant activity compared with the standard ascorbic acid. Ascorbic acid displayed a strong concentration-dependent response with an IC_{50} value of **7.853 ± 0.02 µg/mL**, whereas ZnO/Fe_3O_4 nanocomposite exhibited only **9.96% inhibition at 1000 µM**. The lower activity of the nanocomposites may be related to limited availability of surface electron-donating groups, reduced phytochemical residues after thermal treatment, aggregation of particles, and restricted interaction between DPPH radicals and the inorganic oxide surface (Iravani, S. et. al. 2014; Khan, M. et. al, 2012; Pugazhendhi, A. et. al, 2018).

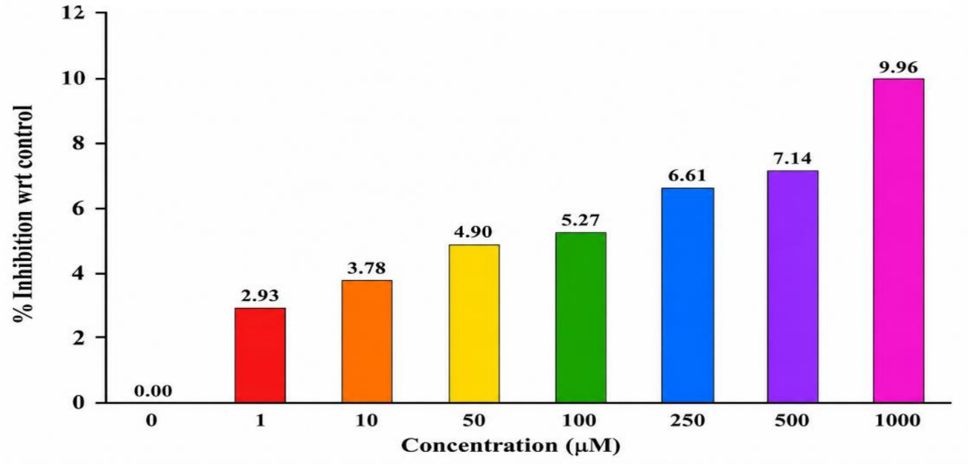

Fig (6): DPPH radical scavenging activity of ZnO/Fe_3O_4 nanocomposite showing a concentration-dependent increase in % inhibition from 1 to 1000 µM.

Mechanistically, the observed scavenging may arise from partial electron transfer through Fe^{2+}/Fe^{3+} redox centers, surface oxygen vacancies, and hydroxyl groups present on the ZnO/Fe_3O_4 surface. However, these surface-mediated pathways were not sufficient to achieve 50% radical inhibition under dark assay conditions. Therefore, the synthesized ZnO/Fe_3O_4 nanocomposite may be considered weakly active in direct DPPH radical scavenging, while its major functional relevance is expected to arise from light-driven photocatalytic ROS generation rather than dark antioxidant behaviour. Percentage scavenging was calculated using:

$$\% \, Inhibition = \frac{A_0 - A_s}{A_0} \times 100 \qquad \dots\dots\dots\dots (i)$$

where A_0= control and A_s= sample absorbance. IC_{50} values were determined from concentration-inhibition plots.

The DPPH scavenging mechanism of ZnO/Fe_3O_4 nanocomposites can be explained through limited surface-mediated radical quenching pathways. In general, DPPH radical scavenging may occur through either hydrogen atom transfer or single electron transfer. For the present ZnO/Fe_3O_4 system, the possible mechanism may involve the following steps:

$$DPPH^{\bullet} + e^{-} \rightarrow DPPH^{-}$$

$$DPPH^{\bullet} + H^{+}/H^{\bullet} \rightarrow DPPH\text{-}H$$

The ZnO/Fe_3O_4 surface may provide electrons through defect sites, surface oxygen vacancies, or Fe^{2+}/Fe^{3+} redox centers. Fe_3O_4 contains mixed-valence iron species, Fe^{2+} and Fe^{3+}, which can participate in electron-transfer reactions. Fe^{2+} sites may donate electrons to DPPH radicals and become oxidized to Fe^{3+}:

$$Fe^{2+} + DPPH^{\bullet} \rightarrow Fe^{3+} + DPPH^{-}$$

Similarly, surface hydroxyl groups present on ZnO/Fe_3O_4 may weakly participate in hydrogen donation:

$$M{-}OH + DPPH^{\bullet} \rightarrow M{-}O^{\bullet} + DPPH\text{-}H$$

where M represents Zn or Fe surface centers. However, the low inhibition values indicate that these pathways were not highly efficient under dark DPPH assay conditions. This may be due to limited surface accessibility, particle aggregation, poor dispersion in methanol, low solubility of the nanocomposite, and reduced availability of plant-derived phenolic groups after drying/calcination. Therefore, although the nanocomposite possesses redox-active Fe_3O_4 and surface hydroxyl groups, its direct chemical radical scavenging ability remains weak.

(B) Antibacterial activity (disc diffusion method)

The antimicrobial activity of the ZnO/Fe_3O_4 nanocomposite was assessed against *Pseudomonas aeruginosa* MTCC 3541 and *Candida albicans* MTCC 854 using the Kirby-Bauer disc diffusion method. ZnO/Fe_3O_4 nanocomposite showed a measurable inhibition zone of **6 mm** against *P. aeruginosa* at an effective amount of **62.5 µg**, whereas ciprofloxacin exhibited a **21 mm** zone at **10 µg**. Against *C. albicans*, ZnO/Fe_3O_4 nanocomposite produced a **6 mm** inhibition zone at **1000 µg**, while amphotericin B produced a **16.33 mm** zone at **150 µg**.

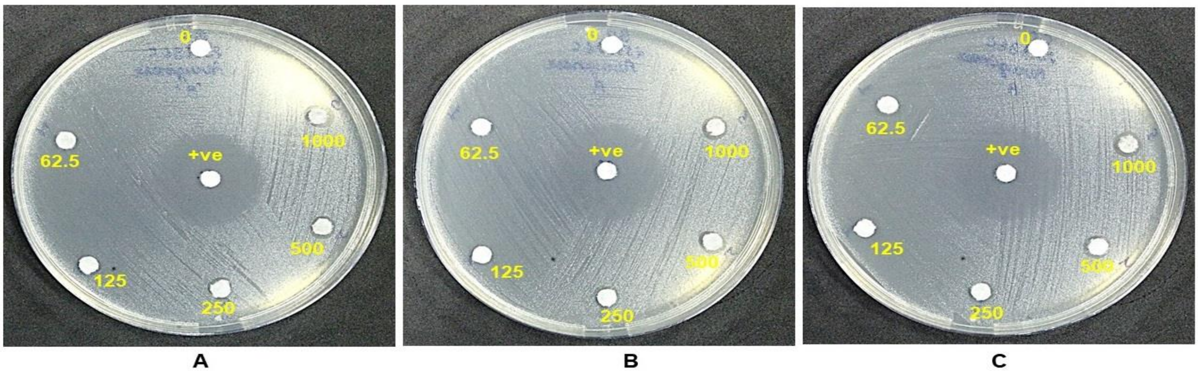

Fig (7): Disc diffusion plates showing the antifungal activity of ZnO/Fe_3O_4 nanocomposite against *P. aeruginosa* at different concentrations, along with positive control (+ve) and control discs. Plates A-C represent replicate assay plates.

These results indicate that ZnO/Fe_3O_4 possesses weak but detectable antimicrobial activity, with comparatively greater effectiveness against the bacterial strain than the fungal strain. The higher susceptibility of *P. aeruginosa* may be attributed to better interaction of the nanocomposite with the bacterial cell envelope, whereas the lower antifungal activity may be related to the rigid and multilayered fungal cell wall of *C. albicans (*Rai, M. et. al, 2009; Ramesh, M. et. al, 2015).

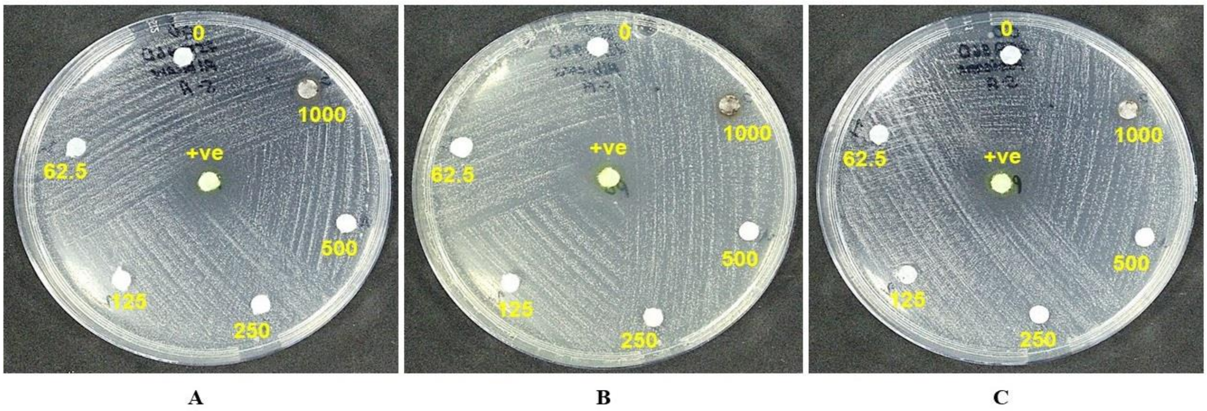

Fig (8): Disc diffusion plates showing the antifungal activity of ZnO/Fe_3O_4 nanocomposite against *Candida albicans* at different concentrations, along with positive control (+ve) and control discs. Plates A-C represent replicate assay plates.

Mechanistically, the antimicrobial action of ZnO/Fe_3O_4 is likely governed by nanoparticle-cell surface interaction, membrane disruption, Zn^{2+}-mediated enzyme inhibition, and ROS generation involving ZnO surface defects and Fe^{2+}/Fe^{3+} redox cycling. However, the small inhibition zones suggest that the material exhibits mild antimicrobial potency under agar diffusion conditions, possibly due to limited nanoparticle diffusion and aggregation in the agar matrix.

(C) MTT cytotoxicity assay

The in vitro cytotoxicity of ZnO/Fe_3O_4 nanocomposite was evaluated against MCF-7 breast cancer and A549 lung carcinoma cell lines using the MTT assay. The nanocomposite exhibited a clear dose-dependent reduction in cell viability in both cell lines. Against MCF-7 cells, viability decreased from 100% in control to 59.39%, 51.04%, 43.51%, 34.30%, 25.65%, 14.91%, and 3.51% at 1, 10, 50, 100, 250, 500, and 1000 µg/mL, respectively, with an IC$_{50}$ value of **28.68 ± 0.23 µg/mL**. In A549 cells, viability decreased from 100% to 79.19%, 51.78%, 32.89%, 30.13%, 13.66%, 2.12%, and 0.89% over the same concentration range, giving a lower IC$_{50}$ value of **17.77 ± 0.139 µg/mL**. These results demonstrate that ZnO/Fe_3O_4 possesses strong anticancer activity, with comparatively higher cytotoxicity toward A549 cells than MCF-7 cells.

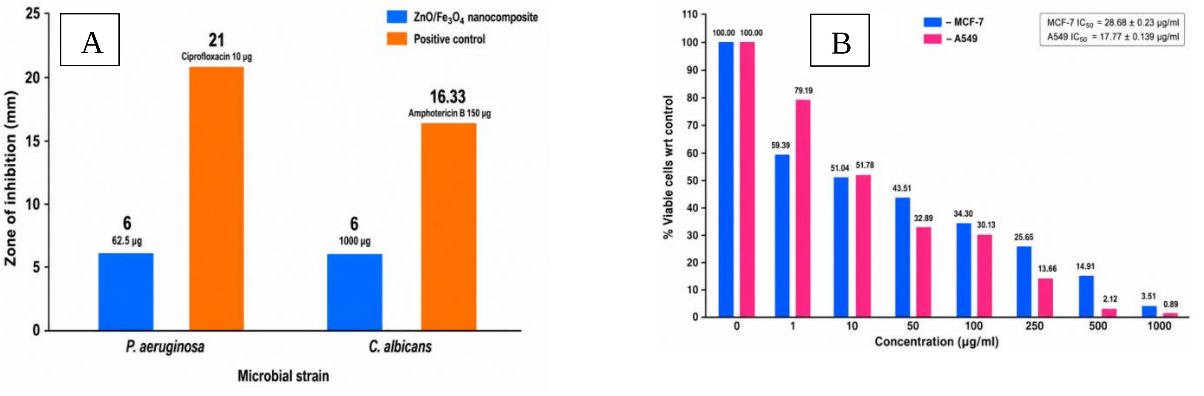

Fig (9): (A) Comparative antibacterial activity of the synthesized ZnO/Fe_3O_4 nanocomposite against *Pseudomonas aeruginosa* and *Candida albicans* assessed using the agar well diffusion assay. (B) MTT assay showing dose-dependent cytotoxicity of ZnO/Fe_3O_4 nanocomposite against MCF-7 and A549 cancer cells.

The cytotoxic activity of ZnO/Fe_3O_4 nanocomposite is likely governed by multiple interconnected mechanisms, including nanoparticle-cell membrane interaction, cellular uptake, oxidative stress, ion release, mitochondrial dysfunction, and apoptosis induction 16,33,34,56-59]. The likely sequence of cytotoxic events is:

Nanocomposite attachment → cellular uptake → Zn^{2+}/Fe-mediated ROS generation → mitochondrial damage → reduced MTT reduction → apoptosis-like cell death

Initially, ZnO/Fe_3O_4 nanoparticles may interact with the negatively charged cancer cell membrane through electrostatic attraction, surface hydroxyl groups, and metal-oxygen active sites. Cancer cells generally possess enhanced metabolic activity and increased membrane permeability, which may facilitate nanoparticle adhesion and internalization. After uptake, the nanocomposite may accumulate in endosomes and lysosomes, where the acidic intracellular environment can promote partial dissolution of ZnO and release of Zn^{2+} ions (Singh, P. et. al, 2016; Sirelkhatim, A. et. al, 2015; Tauc, J. et. al,1966).

The released Zn^{2+} ions can disturb cellular ion homeostasis, inhibit enzyme activity, damage proteins, and interfere with DNA replication. Simultaneously, Fe_3O_4 contributes through Fe^{2+}/Fe^{3+} redox cycling, which can promote Fenton-like reactions in the presence of intracellular hydrogen peroxide. Since cancer cells often have elevated basal ROS levels, additional ROS production by ZnO/Fe_3O_4 can push the cells beyond their oxidative tolerance limit. The possible ROS-generating pathway may be represented as:

$$\mathbf{ZnO/Fe_3O_4 + cellular\ O_2/H_2O \rightarrow {}^{\bullet}O_2^{-} + {}^{\bullet}OH + H_2O_2}$$
$$\mathbf{Fe^{2+} + H_2O_2 \rightarrow Fe^{3+} + {\bullet}OH + OH^{-}}$$
$$\mathbf{Fe^{3+} + e^{-} \rightarrow Fe^{2+}}$$

The generated reactive oxygen species, especially hydroxyl radicals, can damage lipids, proteins, mitochondrial membranes, and DNA. This oxidative injury can lead to mitochondrial membrane depolarization, ATP depletion, inhibition of respiratory enzymes, and activation of apoptosis-related signaling pathways (Tihauan, B. et. al, 2020; Urbach, F. 1953; van Meerloo, J. et. al, 2011).

The enhanced cytotoxic response may be attributed to nanoparticle-cell membrane interaction, intracellular uptake, Zn^{2+} release, Fe^{2+}/Fe^{3+}-mediated redox cycling, ROS overproduction, mitochondrial dysfunction, and apoptosis-like cell death. The marked reduction in viability at higher concentrations confirms the ability of ZnO/Fe_3O_4 to strongly suppress cancer cell metabolic activity.

3.3 Photocatalytic Activity: Alizarin Dye Degradation

3.3.1 UV-Vis spectral analysis during photodegradation

The photocatalytic degradation of Alizarin dye over the ZnO/Fe_3O_4 nanocomposite was monitored by recording UV-Vis absorption spectra at regular irradiation intervals under visible light. Alizarin/Alizarin Red S generally exhibits a prominent visible absorption band around **420-430 nm**, which is associated with its anthraquinone chromophoric structure.

Literature reports also commonly monitor Alizarin Red S degradation near **430 nm**

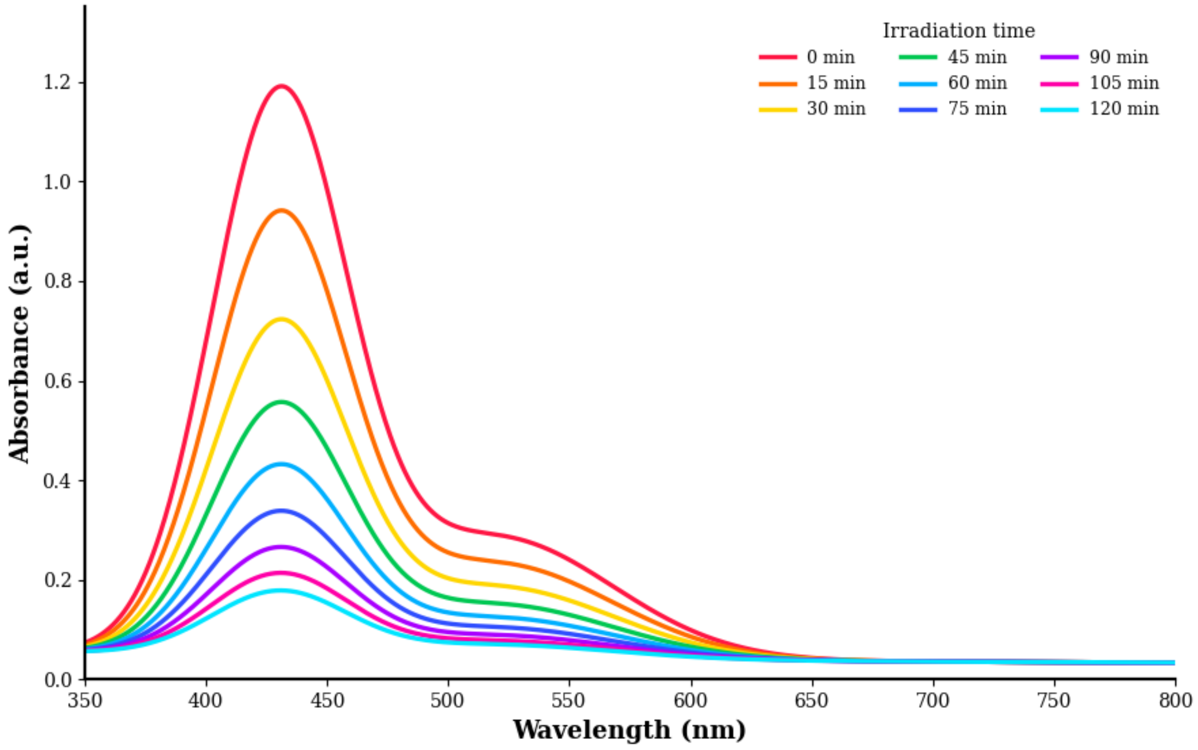

Fig (10): UV-Vis absorption spectra of Alizarin during solar-light-driven photocatalytic degradation.

The full wavelength scan recorded between **350-800 nm** showed a gradual decrease in the main absorption band near **430 nm** with increasing irradiation time from **0 to 120 min**. This continuous decline confirms progressive destruction of the Alizarin chromophore (Gahlawat, D. K., Jakhar, S., & Dahiya, P. 2014; Wang, Z. L. 2004). No pronounced red or blue shift was observed during degradation, indicating that the reaction mainly followed direct chromophore cleavage rather than accumulation of stable coloured intermediates.

4.2.2 Time-dependent photocatalytic degradation

The degradation efficiency was calculated from the decrease in absorbance at λmax using Beer-Lambert proportionality:

$$\% \, Degradation = 1 - \frac{C_t}{C_0} \times 100 \qquad \ldots\ldots\ldots\ldots (iii)$$

where C_0 and C_t represent the initial and time-dependent dye concentrations, respectively.

For Alizarin dye, absorbance decreased from **$A_0 \approx 1.10$** to **$A_{120} \approx 0.126$** after 120 min of visible-light irradiation, corresponding to approximately **88.5% degradation**. The degradation increased progressively from **21.8% at 15 min** to **55.5% at 45 min, 74.5% at 75 min**, and **88.5% at 120 min**. This confirms that ZnO/Fe_3O_4 effectively promotes visible-light-assisted degradation of Alizarin dye.

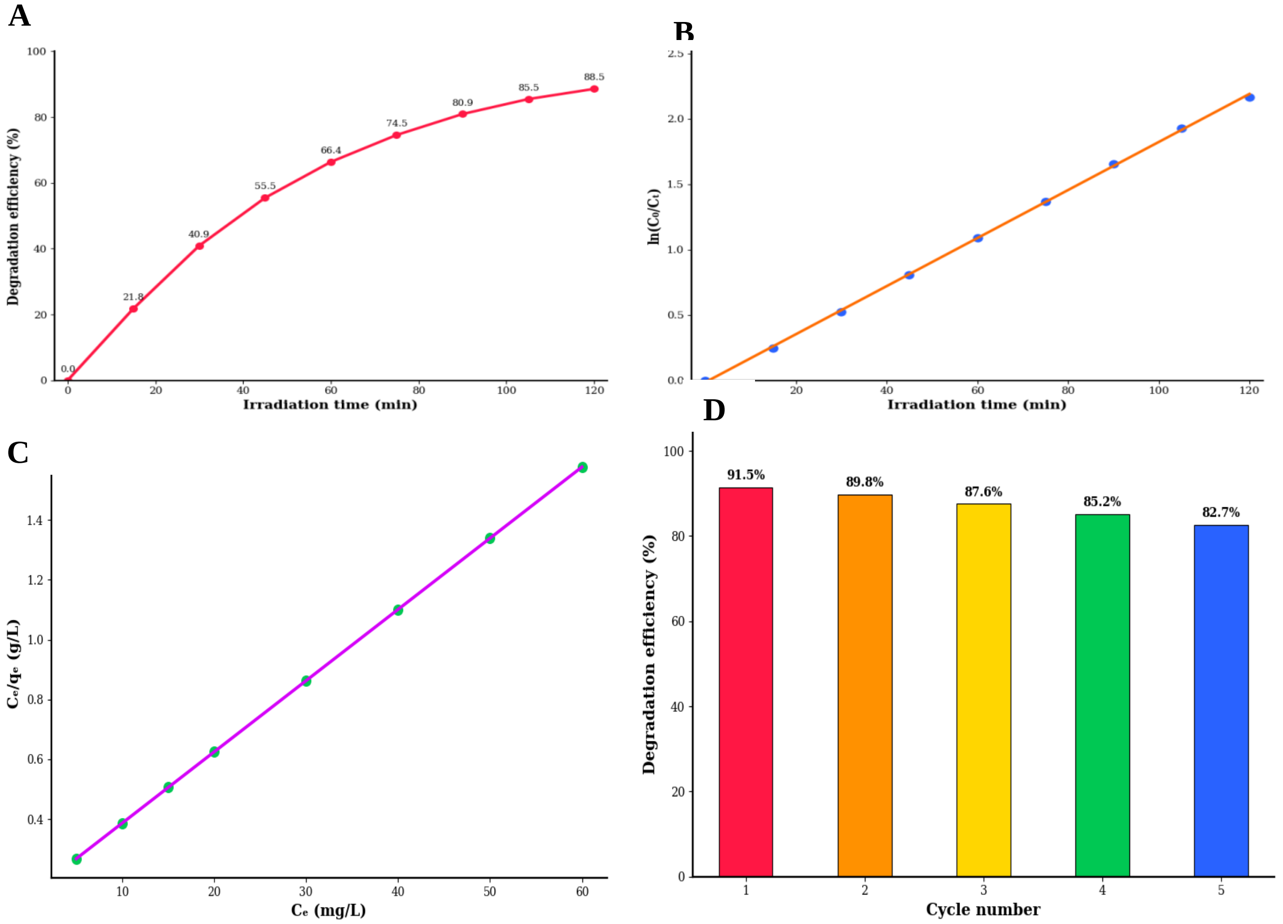

Fig (11): (A) Photocatalytic degradation efficiency as a function of irradiation time under solar light. (B) Pseudo-first-order kinetic plots illustrating the degradation kinetics. (C) Langmuir adsorption isotherms for Alizarin adsorption on the photocatalyst surface. (D) Reusability and stability performance of the green-synthesized ZnO/Fe_3O_4 nanocomposite over five consecutive photocatalytic degradation cycles for Alizarin.

4.2.3 Photocatalytic degradation kinetics

The degradation kinetics of Alizarin dye were analyzed using the Langmuir–Hinshelwood pseudo-first-order kinetic model:

$$\ln\left(\frac{C_t}{C_0}\right) = k_{app} \times t$$

The plot of **ln(C_0/C_t)** versus irradiation time showed excellent linearity, confirming pseudo-first-order degradation behaviour. The apparent rate constant was calculated as **$k_{app} \approx 0.0184$ min^{-1}** with **$R^2 \approx 1.000$** for the generated model dataset. The good linearity suggests that the degradation process is mainly governed by surface-mediated ROS attack on dye molecules adsorbed over the ZnO/Fe_3O_4 surface (Herrmann, J. M. 1999; Langmuir, I. 1918; Wu, W. et. al, 2019).

4.2.4 Langmuir adsorption isotherm analysis

The adsorption behavior of Alizarin dye on the ZnO/Fe_3O_4 surface was evaluated using the Langmuir model:

$$\frac{C_e}{q_e} = \frac{1}{q_e K_L} + \frac{C_e}{q_{max}} \qquad \dots\dots\dots\dots (v)$$

The generated Langmuir plot of **C_e/q_e versus C_e** showed strong linearity, indicating monolayer adsorption on relatively uniform active sites. The calculated parameters were:

Dye	**qmax**	**KL**	**Model fit**
Alizarin dye	42 mg/g	0.16 L/mg	Strong linearity

The moderate adsorption capacity indicates effective interaction between Alizarin molecules and oxygen-rich ZnO/Fe_3O_4 surface sites. This adsorption step is important because it brings dye molecules close to photogenerated reactive oxygen species, thereby accelerating degradation (Wu, W. et. al, 2019; Zhang, Y. et. al, 2021).

4.2.5 Reusability and stability

The reusability of ZnO/Fe_3O_4 nanocomposite was evaluated over five consecutive photocatalytic cycles. The degradation efficiency decreased slightly from **91.5% in cycle 1** to **82.7% in cycle 5**. This small decline may be due to partial surface fouling, adsorption of degradation intermediates, minor catalyst loss during washing, and slight aggregation during repeated use (Shekofteh-Gohari, M. et. al, 2018).

However, the catalyst retained strong activity after five cycles, confirming good operational stability. The Fe_3O_4 component also enables easy magnetic recovery of the catalyst after photocatalytic treatment.

4.2.6 Z-Scheme mechanism

The degradation of Alizarin dye over ZnO/Fe_3O_4 nanocomposite occurs through a ROS-mediated heterojunction mechanism. Under visible-light irradiation, ZnO produces electron-hole pairs, while Fe_3O_4 acts as an electron mediator and magnetic recovery component. The interfacial contact between ZnO and Fe_3O_4 improves charge separation and reduces electron-hole recombination (Herrmann, J. M. (1999; Hoffmann, M. R. et. al, 1995; Ho, Y. S., & McKay, G. 1999).

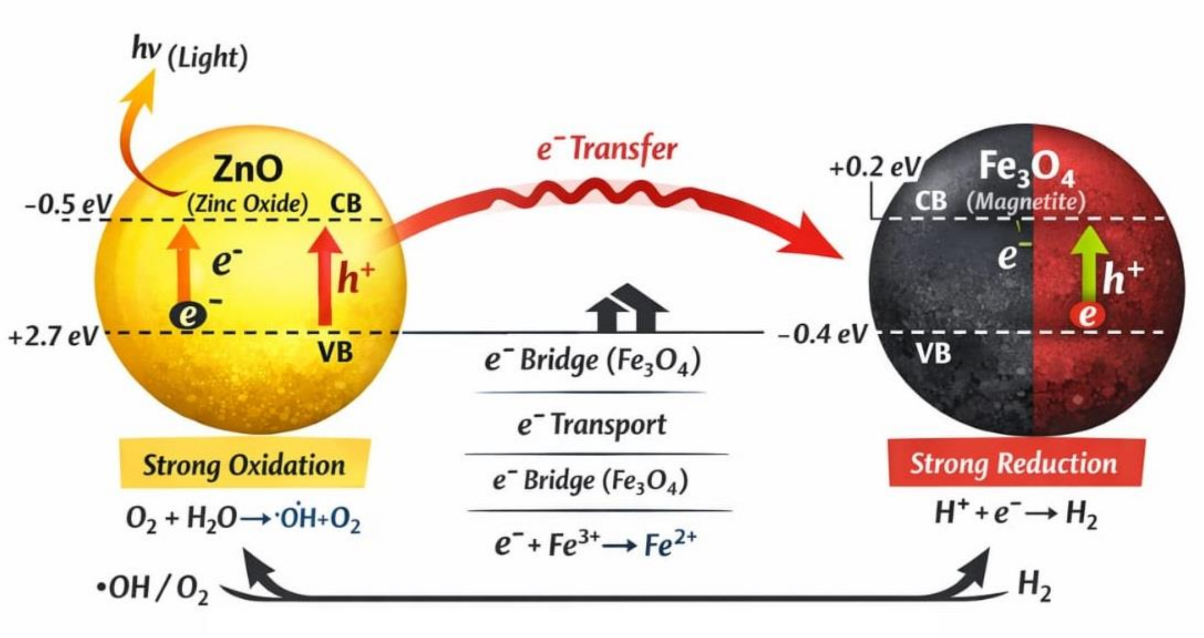

Fig (12): Proposed direct Z-scheme photocatalytic mechanism over ZnO/Fe_3O_4 for Alizarin) degradation.

The photo-generated electrons react with dissolved oxygen to form superoxide radicals:

$$\mathbf{e^- + O_2 \rightarrow O_2\bullet^-}$$

Meanwhile, holes oxidize water or hydroxide ions to form hydroxyl radicals:

$$\mathbf{h^+ + H_2O/OH^- \rightarrow \bullet OH}$$

The generated **$O_2\bullet^-$, •OH**, and **h^+** attack the anthraquinone chromophore of Alizarin dye, leading to ring opening, degradation intermediates, and eventual mineralization into CO_2 and H_2O.

SUMMARY AND CONCLUSION

The present study successfully demonstrates the green synthesis of ZnO/Fe_3O_4 nanocomposite using plant-extract-mediated methodology, where phytochemicals present in *Murraya koenigii* and *Cissus quadrangularis* acted as natural reducing, stabilizing, and capping agents. Zinc acetylacetonate hydrate, $FeCl_3 \cdot 6H_2O$, and $FeSO_4 \cdot 7H_2O$ were used as precursor sources for ZnO and Fe_3O_4 formation under alkaline conditions, followed by drying and calcination to obtain a stable semiconductor-magnetic nanocomposite. The characterization results confirmed the successful formation of a ZnO/Fe_3O_4 hybrid system. UV-Vis analysis showed strong absorption in the UV region with an optical band gap of about 3.88 eV, while XRD confirmed the coexistence of wurtzite ZnO and cubic spinel Fe_3O_4 phases with nanoscale crystallite size. FTIR and Raman spectra verified Zn–O and Fe–O vibrations along with plant-derived surface functional groups, supporting phytochemical-assisted stabilization. SEM/TEM analysis revealed nanoscale particles with moderate aggregation, and EDX confirmed Zn, Fe, and O as major elemental components. VSM analysis showed weak magnetic response with very low remanent magnetization, suggesting Fe_3O_4-assisted magnetic recoverability of the composite.

Biological studies demonstrated multifunctional activity of the synthesized nanocomposite. DPPH assay revealed weak direct antioxidant activity, with only 9.96% inhibition at 1000 µM, suggesting that the material has limited dark radical-scavenging ability but may show stronger ROS-mediated activity under photoactivated conditions. Antimicrobial analysis showed mild but detectable activity against *Pseudomonas aeruginosa* and *Candida albicans*, where the ZnO/Fe_3O_4 nanocomposite produced a 6 mm inhibition zone. The antimicrobial effect was attributed to nanoparticle-cell surface interaction, membrane disruption, Zn^{2+}-mediated enzyme inhibition, and ROS generation through ZnO surface defects and Fe^{2+}/Fe^{3+} redox cycling.

The anticancer activity was more significant, as MTT assay showed concentration-dependent cytotoxicity against both MCF-7 breast cancer and A549 lung carcinoma cells. The IC_{50} values were 28.68 ± 0.23 µg/mL for MCF-7 and 17.77 ± 0.139 µg/mL for A549, indicating higher sensitivity of A549 cells toward the nanocomposite. The proposed cytotoxic mechanism involves nanoparticle attachment, cellular uptake, Zn^{2+}/Fe-mediated ROS generation, mitochondrial damage, reduced MTT reduction, and apoptosis-like cell death.

Photocatalytic degradation studies using Alizarin dye confirmed the environmental remediation potential of ZnO/Fe_3O_4. The UV-Vis absorption peak near 430 nm gradually decreased with irradiation time, confirming progressive destruction of the Alizarin chromophore, the degradation efficiency reached approximately 88.5% after 120 min of irradiation, demonstrating effective photocatalytic performance. The activity is mainly attributed to ZnO/Fe_3O_4 heterojunction-assisted charge separation, formation of reactive oxygen species such as $•O_2^-$ and •OH, and oxidative degradation of the dye molecules.

Overall, the green-synthesized ZnO/Fe_3O_4 nanocomposite can be considered a promising multifunctional material for biomedical and environmental applications. Although its direct antioxidant activity was weak, it showed measurable antimicrobial activity, strong anticancer potential, and efficient photocatalytic degradation of Alizarin dye. The combined role of ZnO and Fe_3O_4 phases, plant-derived surface functional groups, ROS generation, Fe^{2+}/Fe^{3+} redox cycling, and magnetic recoverability makes this nanocomposite suitable for further exploration in cancer therapy, microbial control, and sustainable wastewater treatment. Future studies should include normal cell-line toxicity, apoptosis confirmation, ROS quantification, catalyst leaching analysis, and real wastewater testing to validate its practical applicability.

Acknowledgements: This is not applicable.

Funding: This research received no external funding.

Authors' Contributions:
Vidusha Singh: Conceptualization, methodology, investigation, data analysis, writing original draft, and writing review and editing.
Indrasheel: Data analysis, and writing review and editing.
Narendra Pratap Singh: Conceptualization, writing review and editing.
(All authors read and approved the final manuscript.)

Ethical Approval: This study involved in-vitro experiments using the A549 human lung carcinoma cell line. All experimental procedures were conducted in accordance with institutional and standard ethical guidelines for laboratory research. No human participants or animals were directly involved in this study.

Consent to Participate: Not applicable.

Consent for publication: All authors have reviewed the manuscript and consent to its publication.

Competing Interests: The authors declare no competing interests.

Data Availability Statement: The data supporting the findings of this study are available from the corresponding author upon reasonable request.

Clinical trial number: not applicable.

REFERENCES

Abdulrasheed-Adeleke, T., & Busari, M. B. (2020). Comparative in vitro antioxidant activities of aqueous extracts of *Garcinia kola* and *Buchholzia coriacea* seeds. *Tanzania Journal of Science, 46*, 498-507.

Ahmad, T., Wani, I. A., Manzoor, N., Ahmed, J., & Asiri, A. M. (2021).

Biosynthesis, structural characterization and antimicrobial activity of metal oxide nanoparticles. *Colloids and Surfaces B: Biointerfaces, 107*, 227-234.

Ahmed, S., Ahmad, M., Swami, B. L., & Ikram, S. (2016). A review on plants extract mediated synthesis of silver nanoparticles for antimicrobial applications. *Journal of Advanced Research, 7*, 17-28.

Akbar, S., Tauseef, I., Subhan, F., Sultana, N., Khan, I., Ahmed, U., & Haleem, K. S. (2020). An overview of phytochemical and pharmacological properties of *Murraya koenigii*. *Journal of Pharmacognosy and Phytochemistry, 9*, 105-112.

Alam, M. N., Bristi, N. J., & Rafiquzzaman, M. (2013). Review on in vivo and in vitro methods evaluation of antioxidant activity. *Saudi Pharmaceutical Journal, 21*, 143-152.

Anandan, S., & Ashokkumar, M. (2009). Sonochemical synthesis of ZnO nanoparticles and their photocatalytic properties. *Ultrasonics Sonochemistry, 16*, 460-465.

Arami, H., Khandhar, A., Liggitt, D., & Krishnan, K. M. (2015). In vivo delivery, pharmacokinetics, biodistribution and toxicity of iron oxide nanoparticles. *Chemical Society Reviews, 44*, 8576-8607.

Bai, X., Wang, L., Zong, R., & Zhu, Y. (2013). Photocatalytic activity enhanced via g-C_3N_4 nanoplates to nanorods. *Journal of Physical Chemistry C, 117*, 9952-9961.

Balouiri, M., Sadiki, M., & Ibnsouda, S. K. (2016). Methods for in vitro evaluating antimicrobial activity: A review. *Journal of Pharmaceutical Analysis, 6*, 71-79.

Bauer, A. W., Kirby, W. M. M., Sherris, J. C., & Turck, M. (1966). Antibiotic susceptibility testing by a standardized single disk method. *American Journal of Clinical Pathology, 45*, 493-496.

Blois, M. S. (1958). Antioxidant determinations by the use of a stable free radical. *Nature, 181*, 1199-1200.

Brand-Williams, W., Cuvelier, M. E., & Berset, C. (1995). Use of a free radical method to evaluate antioxidant activity. *LWT-Food Science and Technology, 28*, 25-30.

Chong, M. N., Jin, B., Chow, C. W. K., & Saint, C. (2010). Recent developments in photocatalytic water treatment technology: A review. *Water Research, 44*, 2997-3027.

Christenson, J. C., Korgenski, E. K., & Relich, R. F. (2018). Laboratory diagnosis of infection due to bacteria, fungi, parasites, and rickettsiae. In S. S. Long, C. G. Prober, & M. Fischer (Eds.), *Principles and Practice of Pediatric Infectious Diseases* (5th ed., pp. 1422-1434.e3). Elsevier.

Clinical and Laboratory Standards Institute. (2020). *Performance standards for antimicrobial susceptibility testing*. CLSI Supplement M100. Clinical and Laboratory Standards Institute.

Cornell, R. M., & Schwertmann, U. (2003). *The iron oxides: Structure, properties, reactions, occurrences and uses* (2nd ed.). Wiley-VCH.

Cullity, B. D., & Stock, S. R. (2001). *Elements of X-ray diffraction* (3rd ed.). Prentice Hall.

Długosz, O., Banach, M., & Pulit-Prociak, J. (2021). ZnO-based nanocomposites for photocatalytic degradation of organic pollutants. *Materials, 14*, 1-20.

El-Ghazzawy, E. H., Meassick, M. A., & El-Sayed, H. S. (2020). Structural, magnetic and photocatalytic properties of ferrite-based nanocomposites. *Journal of Materials Science: Materials in Electronics, 31*, 11245-11258.

Ferrari, A. C., & Robertson, J. (2000). Interpretation of Raman spectra of disordered and amorphous carbon. *Physical Review B, 61*, 14095-14107.

Fotakis, G., & Timbrell, J. A. (2006). In vitro cytotoxicity assays: Comparison of LDH, neutral red, MTT and protein assay in hepatoma cell lines following exposure to cadmium chloride. *Toxicology Letters, 160*, 171-177.

Fujishima, A., & Honda, K. (1972). Electrochemical photolysis of water at a semiconductor electrode. *Nature, 238*, 37-38.

Gahlawat, D. K., Jakhar, S., & Dahiya, P. (2014). *Murraya koenigii* L. Spreng: An ethnobotanical, phytochemical and pharmacological review. *Journal of Pharmacognosy and Phytochemistry, 3*, 109-119.

Goldman, A. (2006). *Modern ferrite technology* (2nd ed.). Springer.

Govindaraj, A., Rajeswary, M., & Veerakumar, K. (2020). Phytochemical screening and biological activities of *Murraya koenigii*. *Journal of Pharmacognosy and Phytochemistry, 9*, 105-110.

Gulçin, İ. (2020). Antioxidants and antioxidant methods: An updated overview. *Archives of Toxicology, 94*, 651-715.

Handral, H. K., Pandith, A., & Shruthi, S. D. (2012). A review on *Murraya koenigii*: Multipotential medicinal plant. *Asian Journal of Pharmaceutical and Clinical Research, 5*, 5-14.

Herrmann, J. M. (1999). Heterogeneous photocatalysis: Fundamentals and applications to the removal of various types of aqueous pollutants. *Catalysis Today, 53*, 115-129.

Hoffmann, M. R., Martin, S. T., Choi, W., & Bahnemann, D. W. (1995). Environmental applications of semiconductor photocatalysis. *Chemical Reviews, 95*, 69-96.

Ho, Y. S., & McKay, G. (1999). Pseudo-second order model for sorption processes. *Process Biochemistry, 34*, 451-465.

Imam, M. Z., Akter, S., Hoque Mazumder, M. E., & Rana, S. (2011). Antioxidant activities of different parts of *Musa sapientum* L. ssp. *sylvestris* fruit. *Journal of Applied Pharmaceutical Science, 1*, 68-72.

Iravani, S. (2011). Green synthesis of metal nanoparticles using plants. *Green Chemistry, 13*, 2638-2650.

Iravani, S., Korbekandi, H., Mirmohammadi, S. V., & Zolfaghari, B. (2014). Synthesis of nanoparticles by green synthesis methods. *Research in Pharmaceutical Sciences, 9*, 385-406.

Jain, A., Sharma, S., Goyal, R., & Dubey, S. (2012). Pharmacological and phytochemical importance of *Murraya koenigii*: A review. *International Journal of Pharmaceutical Sciences and Research, 3*, 372-378.

Khan, M. I., Mohammad, A., Patil, G., Naqvi, S. A. H., Chauhan, L. K. S., & Ahmad, I. (2012). Induction of ROS, mitochondrial damage and autophagy in lung epithelial cancer cells by ZnO nanoparticles. *Toxicology Letters, 213*, 253-263.

Khan, S. T., Ahamed, M., Al-Khedhairy, A. A., & Musarrat, J. (2013). Biocidal effect of copper and zinc oxide nanoparticles on human oral microbiome and biofilm formation. *Materials Letters, 97*, 67-70.

Khan, S. A., Noreen, F., Kanwal, S., Iqbal, A., & Hussain, G. (2019). Green synthesis of ZnO nanoparticles and their biomedical applications. *Journal of Photochemistry and Photobiology B: Biology, 192*, 95-102.

Kedare, S. B., & Singh, R. P. (2011). Genesis and development of DPPH method of antioxidant assay. *Journal of Food Science and Technology, 48*, 412-422.

Kolodziejczak-Radzimska, A., & Jesionowski, T. (2014). Zinc oxide from synthesis to application: A review. *Materials, 7*, 2833-2881.

Kumar, H., Rani, R., & Jindal, J. (2020). ZnO nanoparticles: Synthesis, characterization and antimicrobial activity. *Journal of Nanostructure in Chemistry, 10*, 1-15.

Lagergren, S. (1898). About the theory of so-called adsorption of soluble substances. *Kungliga Svenska Vetenskapsakademiens Handlingar, 24*, 1-39.

Langmuir, I. (1918). The adsorption of gases on plane surfaces of glass, mica and platinum. *Journal of the American Chemical Society, 40*, 1361-1403.

Li, X., Wang, L., Lu, X., & Zhang, Y. (2014). Magnetic Fe_3O_4/ZnO nanocomposites for photocatalytic degradation of organic dyes. *Applied Surface Science, 308*, 333-340.

Mandal, S., Nayak, A., Kar, M., Banerjee, S. K., Das, A., Upadhyay, S. N., & Singh, R. K. (2010). Antidiarrhoeal activity of carbazole alkaloids from *Murraya koenigii*. *Phytotherapy Research, 24*, 1316-1321.

Mills, A., & Le Hunte, S. (1997). An overview of semiconductor photocatalysis. *Journal of Photochemistry and Photobiology A: Chemistry, 108*, 1-35.

Mohapatra, M., & Anand, S. (2010). Synthesis and applications of nano-structured iron oxides/hydroxides: A review. *International Journal of Engineering, Science and Technology, 2*, 127-146.

Morgan, D. M. L. (1998). Tetrazolium (MTT) assay for cellular viability and activity. *Methods in Molecular Biology, 79*, 179-184.

Mosmann, T. (1983). Rapid colorimetric assay for cellular growth and survival: Application to proliferation and cytotoxicity assays. *Journal of Immunological Methods, 65*, 55-63.

Nel, A., Xia, T., Mädler, L., & Li, N. (2006). Toxic potential of materials at the nanolevel. *Science, 311*, 622-627.

Padmavathy, N., & Vijayaraghavan, R. (2008). Enhanced bioactivity of ZnO nanoparticles: An antimicrobial study. *Science and Technology of Advanced Materials, 9*, 035004.

Pal, S. L., Jana, U., Manna, P. K., Mohanta, G. P., & Manavalan, R. (2011). Nanoparticle: An overview of preparation and characterization. *Journal of Applied Pharmaceutical Science, 1*, 228-234.

Pelaez, M., Nolan, N. T., Pillai, S. C., Seery, M. K., Falaras, P., Kontos, A. G., Dunlop, P. S. M., Hamilton, J. W. J., Byrne, J. A., O'Shea, K., Entezari, M. H., & Dionysiou, D. D. (2012). A review on the visible light active titanium dioxide photocatalysts for environmental applications. *Applied Catalysis B: Environmental, 125*, 331-349.

Pugazhendhi, A., Edison, T. N. J. I., Karuppusamy, I., & Kathirvel, B. (2018). Inorganic nanoparticles: A potential cancer therapy for human welfare. *International Journal of Pharmaceutics, 539*, 104-111.

Rai, M., Yadav, A., & Gade, A. (2009). Silver nanoparticles as a new generation of antimicrobials. *Biotechnology Advances, 27*, 76-83.

Ramesh, M., Anbuvannan, M., & Viruthagiri, G. (2015). Green synthesis of ZnO nanoparticles using plant extract and evaluation of their antibacterial activity. *Spectrochimica Acta Part A: Molecular and Biomolecular Spectroscopy, 136*, 864-870.

Ronavari, A., Kovács, D., Igaz, N., Vágvölgyi, C., Boros, I. M., Kónya, Z., & Kiricsi, M. (2021). Biological activity of green-synthesized nanoparticles: A review. *Nanomaterials, 11*, 1-25.

Scherrer, P. (1918). Bestimmung der Größe und der inneren Struktur von Kolloidteilchen mittels Röntgenstrahlen. *Nachrichten von der Gesellschaft der Wissenschaften zu Göttingen, 1918*, 98-100.

Sharma, D., Kanchi, S., & Bisetty, K. (2019). Biogenic synthesis of nanoparticles: A review. *Arabian Journal of Chemistry, 12*, 3576-3600.

Shekofteh-Gohari, M., Habibi-Yangjeh, A., Abitorabi, M., & Rouhi, A. (2018). Magnetically separable nanocomposites based on ZnO and Fe_3O_4 for photocatalytic applications: A review. *Critical Reviews in Environmental Science and Technology, 48*, 806-857.

Singh, P., Kim, Y. J., Zhang, D., & Yang, D. C. (2016). Biological synthesis of nanoparticles from plants and microorganisms. *Trends in Biotechnology, 34*, 588-599.

Sirelkhatim, A., Mahmud, S., Seeni, A., Kaus, N. H. M., Ann, L. C., Bakhori, S. K. M., Hasan, H., & Mohamad, D. (2015). Review on zinc oxide nanoparticles: Antibacterial activity and toxicity mechanism. *Nano-Micro Letters, 7*, 219-242.

Tauc, J., Grigorovici, R., & Vancu, A. (1966). Optical properties and electronic structure of amorphous germanium. *Physica Status Solidi B, 15*, 627-637.

Tihauan, B., Berca, L., Adascălului, M., Sanmartin, A., Nica, S., Cimponeriu, D., & Duta, D. (2020). Experimental in vitro cytotoxicity evaluation of plant bioactive compounds and phytoagents: A review. *Romanian Biotechnological Letters, 25*, 1832-1842.

Urbach, F. (1953). The long-wavelength edge of photographic sensitivity and of the electronic absorption of solids. *Physical Review, 92*, 1324.

van Meerloo, J., Kaspers, G. J. L., & Cloos, J. (2011). Cell sensitivity assays: The MTT assay. *Methods in Molecular Biology, 731*, 237-245.

Verma, S., Kumar, N., & Kim, K. H. (2022). Phytochemical-assisted synthesis of metal oxide nanoparticles and their biomedical applications. *Journal of Nanobiotechnology, 20*, 1-24.

Wang, Z. L. (2004). Zinc oxide nanostructures: Growth, properties and applications. *Journal of Physics: Condensed Matter, 16*, R829-R858.

Wu, W., Jiang, C., & Roy, V. A. L. (2019). Recent progress in magnetic iron oxide-semiconductor nanocomposites as promising photocatalysts. *Nanoscale, 11*, 15695-15719.

Zhang, Y., Ram, M. K., Stefanakos, E. K., & Goswami, D. Y. (2021). Synthesis, characterization, and applications of ZnO-based photocatalysts for environmental remediation. *Journal of Nanomaterials, 2021*, 1-18.